

Integrated Image Reconstruction and Target Recognition based on Deep Learning Technique

Cien Zhang
Wharton Research Data Services
University of Pennsylvania
Philadelphia, USA
cienzhang@alumni.upenn.edu

Jiaming Zhang
Centre for Wireless Innovation
Queen's University Belfast
Belfast, United Kingdom
jzhang57@qub.ac.uk

Jiajun He
Department of Electrical Engineering
City University of Hong Kong
Hong Kong, China
jjiajunhe5-c@my.cityu.edu.hk

Okan Yurduseven
Centre for Wireless Innovation
Queen's University Belfast
Belfast, United Kingdom
okan.yurduseven@qub.ac.uk

Abstract—Computational microwave imaging (CMI) has gained attention as an alternative technique for conventional microwave imaging techniques, addressing their limitations such as hardware-intensive physical layer and slow data collection acquisition speed to name a few. Despite these advantages, CMI still encounters notable computational bottlenecks, especially during the image reconstruction stage. In this setting, both image recovery and object classification present significant processing demands. To address these challenges, our previous work introduced ClassiGAN, which is a generative deep learning model designed to simultaneously reconstruct images and classify targets using only back-scattered signals. In this study, we build upon that framework by incorporating attention gate modules into ClassiGAN. These modules are intended to refine feature extraction and improve the identification of relevant information. By dynamically focusing on important features and suppressing irrelevant ones, the attention mechanism enhances the overall model performance. The proposed architecture, named Att-ClassiGAN, significantly reduces the reconstruction time compared to traditional CMI approaches. Furthermore, it outperforms current advanced methods, delivering improved Normalized Mean Squared Error (NMSE), higher Structural Similarity Index (SSIM), and better classification outcomes for the reconstructed targets.

Index Terms—computational imaging, deep learning, image reconstruction.

I. INTRODUCTION

Microwave imaging has found extensive use in multiple fields, such as security screening [1]–[3], object localization [4]–[9], medical imaging [10], and space debris detection [11]. One of its main benefits is the ability to penetrate materials that are opaque to visible light. Furthermore, microwave radiation is non-ionizing, which makes it safer for human exposure compared to ionizing alternatives [12]. Conventional microwave imaging methods predominantly employ synthetic aperture radar (SAR) systems [13], which typically require raster scanning at the Nyquist rate [14]. This technique involves sequentially probing the imaging area point by point,

leading to slow data acquisition speed and increased hardware demands. These limitations hinder the feasibility of real-time imaging, particularly for scenes with large electrical dimensions [3], [15], [16].

To address these limitations, computational microwave imaging (CMI) has emerged as an alternative approach. CMI systems utilize spatially incoherent radiation patterns to encode the scene information, thereby reducing dependence on hardware-intensive scanning procedures. These techniques can be broadly categorized into three types: reconfigurable aperture systems [17]–[19], frequency-diverse systems [20]–[22], and hybrid systems that integrate both reconfigurability and frequency diversity [23]. Reconfigurable aperture-based CMI systems make use of antennas with reconfigurable elements. These antennas leverage tunable mechanisms to activate or deactivate the radiating elements, generating diverse radiation patterns [19]. This approach can eliminate the need for sweeping a frequency band, thus enabling even a single frequency operation [24]. However, these systems often require additional circuitry to control the switching states of the radiating elements. In contrast, frequency-diverse CMI systems primarily utilize passive structures that generate varying radiation patterns across different frequencies, eliminating the need for active switching circuits.

While CMI systems effectively reduce hardware complexity through a physical-layer compression, they are still limited by a substantial computational burden. This is because image reconstruction and target classification tasks demand significant processing resources, particularly for electrically large apertures or imaging scenes [25]. To enhance computational efficiency in microwave imaging, including CMI systems, deep learning techniques have been increasingly explored to accelerate the reconstruction process. Several deep learning-based approaches have been developed to address either image reconstruction [26]–[28] or target recognition [29] directly from measured signals. More recent studies have sought to integrate different tasks within a unified framework. For example, the

This work was supported by the Leverhulme Trust under Research Leadership Award RL-2019-019.

work in [30] proposed a convolutional neural network (CNN) [31] architecture with shared layers to jointly extract features from both microwave and ultrasonic data, facilitating accurate target reconstruction and scene segmentation. Similarly, [32] introduced a cascaded CNN structure for simultaneous image super-resolution and target classification in radar imaging. Furthermore, [33] presented a deep learning model capable of reconstructing and classifying imaging targets by leveraging a combination of microwave data, optical images, and corresponding reconstructed outputs. However, the reliance on optical images constrains the practical applicability of this approach, as such data may not always be available.

To address this limitation, our previous work introduced ClassiGAN, a novel Generative Adversarial Network (GAN)-based model that simultaneously performs image reconstruction and target classification using only back-scattered signal measurements [34]. Building on this foundation, the present study further advances the architectural design and performance of ClassiGAN to enhance its applicability, where the proposed model is called Att-ClassiGAN.

The remainder of this article is structured as follows: Section II provides an overview of the CMI system setup. Section III details the proposed network architecture. Experimental results and comparative analyses of the proposed Att-ClassiGAN approach are presented in Section IV. Finally, conclusions are given in Section V.

II. CMI SYSTEM DESCRIPTION

The CMI system used in this study is based on the design presented in [35]. It comprises two two-dimensional (2D) frequency-diverse metasurface antennas arranged in a bistatic configuration, which is shown in Fig. 1. Each metasurface antenna panel features a single feeding port and is populated with a set of complementary electric inductive-capacitive (cELC) unit cells, which are randomly distributed across the aperture. These unit cells maintain a fixed length of 5 mm, while their widths vary between 2 mm and 5 mm, resulting in resonant frequency shifts within the X-band (8–12 GHz). The panels were fabricated using 3.175 mm thick Rogers TMM3 substrates with copper plating, characterized by a relative permittivity $\epsilon_r = 3.45$ and a loss tangent of $\tan \delta = 0.002$.

The CMI working mechanism in this work is shown in Fig. 2. Utilizing the first Born approximation [36], the back-scattered measurement vector \mathbf{g} can be expressed as:

$$\mathbf{g}_{M \times 1} = \mathbf{H}_{M \times N} \boldsymbol{\rho}_{N \times 1} + \mathbf{n}_{M \times 1}, \quad (1)$$

where \mathbf{g} represents the back-scattered signal vector, \mathbf{H} denotes the sensing matrix, and $\boldsymbol{\rho}$ denotes the reflectivity of the scene. The term \mathbf{n} accounts for measurement noise. In (1), the signal vector \mathbf{g} has a size of $M \times 1$, where M denotes the number of measurement modes. Similarly, the vector $\boldsymbol{\rho}$ has a size of $N \times 1$, where N indicates the total number of pixels into which the imaged scene is discretized. In addition, \mathbf{H} is proportional to the dot product of the electromagnetic fields radiated by the transmit and receive antennas, both of which are propagated to the imaged scene [37].

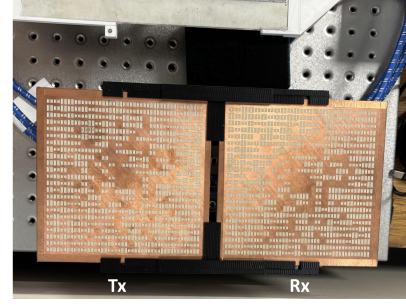


Fig. 1. Front view of the antenna presented in [34].

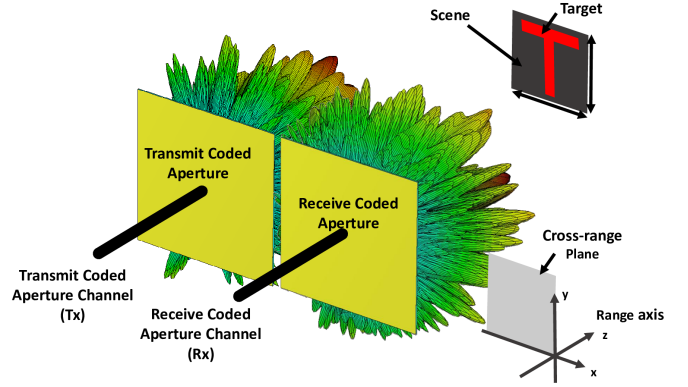


Fig. 2. Coded-aperture CMI setup operating in a bi-static mode. The figure shows the alphabet “T” as the synthetic imaging target.

To reconstruct the scene reflectivity ρ_{rec} , various inversion methods can be employed. One approach is an iterative least-squares optimization, which can be used to estimate the reflectivity $\rho_{\text{rec}}^{\text{LS}}$ and given by:

$$\rho_{\text{rec}}^{\text{LS}} = \arg \min \rho \|\mathbf{g} - \mathbf{H}\rho\|_2^2, \quad (2)$$

where $\|\cdot\|_2$ indicates the L2 norm.

In this work, a hybrid CMI-SAR approach [38] was employed to gather sufficient scene information, enabling high-resolution image reconstructions. Specifically, the measurement grid consists of 16 positions, each spaced 8 cm apart along both the x - and y -axes. Since there are 64 measurement modes used for CI measuring, this work considers $M = 64 \times 16 = 1024$ measurement modes in total.

III. PROPOSED METHOD

A. Network Architecture

Similar to the original ClassiGAN, the developed Att-ClassiGAN also consists of two networks, namely generator and discriminator. The generator is responsible for simultaneously predicting the image reconstructions and the categories of the inputted back-scattered signal, while the discriminator is to verify the authenticity of the inputted image reconstructions. Therefore, after the training process, only the generator will be used during the testing phase. The generator and discriminator are trained alternatively. During the training process, when the generator is being updated, the parameters of the

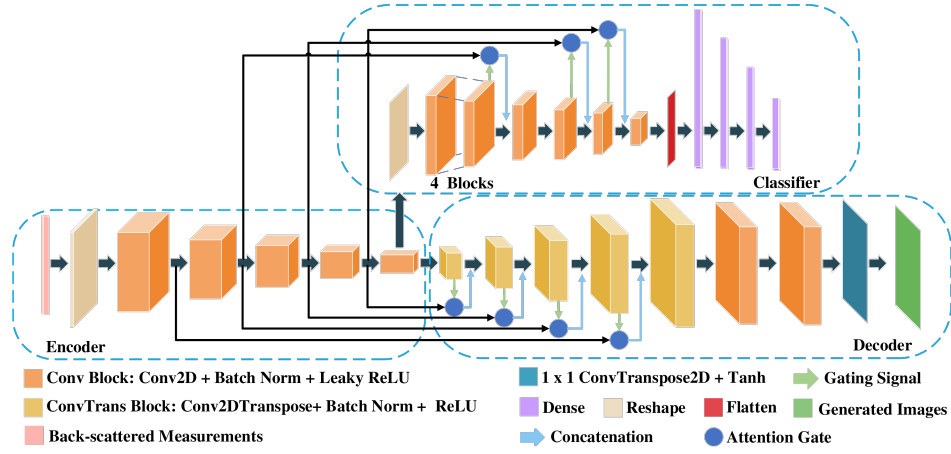


Fig. 3. Architecture of the generator of the Att-ClassiGAN.

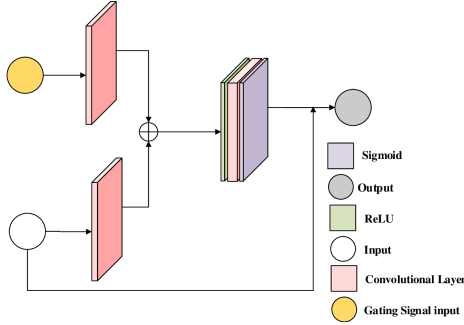


Fig. 4. Working Mechanism of the attention gate module.

discriminator are held constant. Conversely, when optimizing the discriminator, the generator's parameters remain fixed.

The architecture of the Att-ClassiGAN generator is shown in Fig. 3. The generator consists of an encoder and a decoder. The discriminator shares the same architecture as the encoder. The input of the generator is the back-scattered signal, and the outputs are the predicted image reconstruction and its category. The input of the discriminator is either the predicted or ground-truth image reconstruction, and the output is the possibility that inputted image is ground-truth. Considering that the back-scattered measured signal is complex-valued, the real and imaginary components are separated into two channels. Therefore, the input size of the generator is 1024×2 .

The imaged targets considered in this work are hand-written numbers from the publicly accessible dataset MNIST [39]. Considering the Att-ClassiGAN is used to reconstruct images with a size of 28×28 , the output sizes of the generator are 1 for the classification task output and 28×28 for the image reconstruction task output, where the image reconstruction output is consistent with the original resolution of the MNIST images, ensuring compatibility and preserving image fidelity.

Although the original ClassiGAN can perform well in this multi-tasking, to enhance the efficiency of computation, an attention module, attention gate (AG) is employed. By using

the AG, the information for specific tasks can be further extracted from the information in the back-scattered measured signal. The working mechanism is shown in Fig. 4.

As illustrated in Fig. 4, the AG module receives two inputs: the gating signal and the AG input. Each input is first processed by a 1×1 convolutional layer, respectively. After that, the resulting feature maps are summed element-wise. The combined result is then passed through a ReLU activation function, followed by another 1×1 convolutional layer and a sigmoid activation function. This sequence produces an AG ratio, a scalar value ranging between 0 and 1, which represents the relative importance of the AG input features. Finally, this AG ratio is multiplied element-wise with the AG input to generate the AG output. The AG ratio effectively modulates the input features, enhancing relevant information while suppressing redundant information, thereby improving the overall representational efficiency of the module.

The loss function for the discriminator is given by:

$$\mathcal{L}_D = -\mathbb{E}_{\mathbf{g}, G(\mathbf{g})} [\log(1 - D(\mathbf{g}, G(\mathbf{g})))] - \mathbb{E}_{\mathbf{g}, \rho_{\text{rec}}} [\log(D(\mathbf{g}, \rho_{\text{rec}}))], \quad (3)$$

where \mathbb{E} denotes mathematical expectation, $D(\cdot)$ denotes the discriminator's estimated probability that an input image is authentic, and $G(\cdot)$ refers to the reconstructed image.

The generator's loss function consists of two components that correspond to two tasks, where one is related to the classification task and the other concerns image reconstruction. The loss function corresponding to the classification task, which is the categorical cross-entropy function [40], is given by:

$$\mathcal{L}_{CAT} = \mathbb{E}_{l, c} [l \log(c) + (1 - l) \log(c)], \quad (4)$$

where l and c represent the true labels and predicted classes, respectively. The loss function corresponding to the image reconstruction is given by:

$$\mathcal{L}_{IMG} = \lambda \mathcal{L}_{L1} - \mathbb{E}_{\mathbf{g}, G(\mathbf{g})} [\log(D(\mathbf{g}, G(\mathbf{g})))], \quad (5)$$

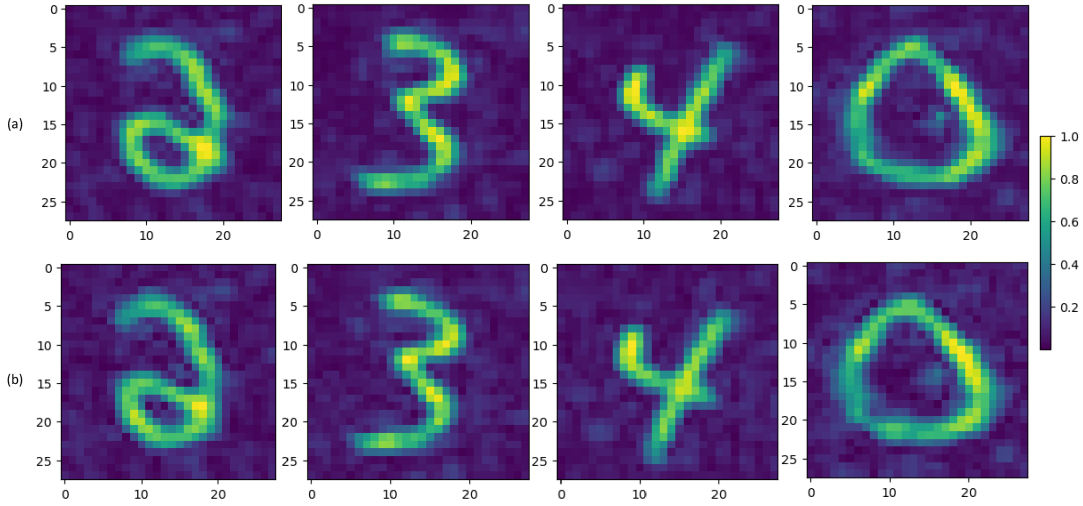


Fig. 5. Comparison of image reconstructions from numerically synthesized data using the experimentally measured sensing matrix: (a) generated by the optimal generator of Att-ClassiGAN, and (b) obtained through conventional methods described in (2).

where

$$\mathcal{L}_{L_1} = \mathbb{E}_{\rho_{\text{rec}}, G(\mathbf{g})} [\|\rho_{\text{rec}} - G(\mathbf{g})\|_1]. \quad (6)$$

The reason why the L1-Norm $\|\cdot\|_1$ is used with a weighting coefficient λ in (5) is that it can support to minimize the element-wise error between the predicted and ground-truth image reconstructions. For the selection of the value of λ , 100 was found to be a proper value in several studies [33], [41], [42].

As discussed in [43], [44], the performance of multi-task networks is highly sensitive to the choice of task-specific loss weights, and manually determining the optimal values can be extremely time-consuming. To alleviate this issue, the uncertainty-weighted loss formulation proposed in [43] is employed. This approach is grounded in the assumptions of Gaussian likelihood for regression tasks and SoftMax likelihood for classification tasks. Although the specific tasks addressed in [43] differ from those studied in the Att-ClassiGAN, the underlying formulation is sufficiently general to be extended to various combinations of discrete and continuous loss functions. Accordingly, the adaptive loss function used to train the generator is defined as follows:

$$\mathcal{L}_G = \frac{1}{(\sigma_1)^2} \mathcal{L}_{CAT} + \frac{1}{2(\sigma_2)^2} \mathcal{L}_{IMG} + \log(\sigma_1) + \log(\sigma_2), \quad (7)$$

where σ_1 and σ_2 are trainable parameters corresponding to the classification and image reconstruction tasks, respectively. A logarithmic transformation is applied to both σ_1 and σ_2 to prevent the loss values from prematurely collapsing to zero during the early stages of training. The presence of the factor 2 alongside $(\sigma_2)^2$ in the image reconstruction loss term \mathcal{L}_{IMG} arises from its derivation under the Gaussian likelihood assumption. Notably, σ_1 and σ_2 are initialized with the same value and updated jointly with the other trainable parameters in the Att-ClassiGAN throughout the training process.

IV. EXPERIMENT VALIDATION

A. Experiment Setup

One data sample consists of a back-scattered measurement, a related image reconstruction and a class. There are 60,000 data samples employed for training and 3,000 data samples used for testing. The initial values of all convolutional filters used in the Att-ClassiGAN are generated by the Xavier initialization method. Each 2D convolutional (Conv2D) layer in the encoder consists of 256 convolutional filters. Additionally, each 2D transpose convolutional (Conv2DTranspose) and Conv2D layer in the decoder contains 64 filters, which is half the number used in the original ClassiGAN. Similarly, the number of convolutional filters in each Conv2D layer of the classifier is also reduced to half of the original.

To enhance computational efficiency during model training, the input data is normalized, as outlined in [45], which follows a standard normal distribution, with zero mean and unit variance before being processed by Att-ClassiGAN. All training and evaluation tasks are executed on a CUDA-enabled platform equipped with an NVIDIA Quadro RTX A5000 GPU, featuring 16 GB of dedicated memory. The entire network, including parameters associated with the adaptive loss function, is trained using the Adam optimization algorithm [46], with a learning rate set to 5×10^{-4} .

B. Results and Discussion

For the image reconstruction task, several results are selected to be shown in Fig. 5. An average normalized mean squared error (NMSE) [47] and Structural Similarity (SSIM) [48] are used to assess the predicted image reconstruction quality. In addition, the average values of precision score, recall score and F1-score are used to evaluate the classification performance. As shown in Table I, with the testing dataset, the average NMSE and SSIM are calculated to be 0.018 and 0.983, which are both superior than those calculated for the

results obtained using the original ClassiGAN. In addition to image reconstruction, the model's classification capability is also evaluated. As illustrated in Fig. 6, the precision score, recall score and F1-score of the classification task are 0.980, which is approximately equal to the values achieved by the original ClassiGAN but with a smaller scale network. These results demonstrate that the AG module effectively enhances information learning and transfer within the network.

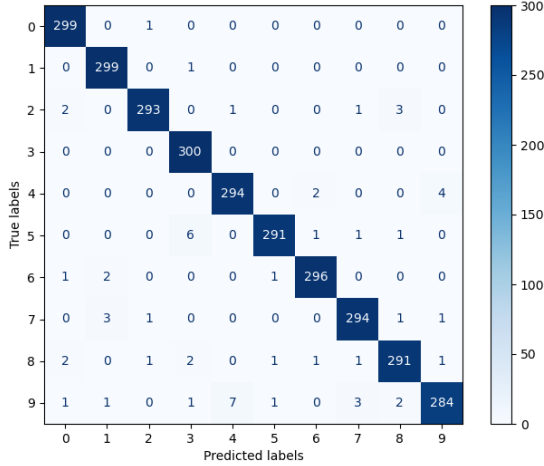


Fig. 6. The confusion matrix for the classification task based on the testing dataset.

Table I also presents a comparative analysis with existing methods. The multi-task learning approaches considered include I-CNN [32], B-CNN [30], and EAVMF [33]. In comparison, Att-ClassiGAN achieves the lowest NMSE and the highest SSIM for the image reconstruction task, while also attaining superior performance in classification metrics, including accuracy, recall, and F1-score. Notably, Att-ClassiGAN exhibits the shortest inference time among all methods, demonstrating its high computational efficiency.

To assess computational efficiency, we also compare the average image reconstruction time. The traditional method described in (2) requires 2.424 seconds per reconstruction, while Att-ClassiGAN significantly reduces this to just 0.059 seconds, which demonstrates a 97.57% reduction. Moreover, compared to the original ClassiGAN, Att-ClassiGAN delivers similar performance with reduced computation time, highlighting its improved efficiency.

TABLE I
COMPARISON OF THE PERFORMANCE OF DIFFERENT METHODS

Method	I-CNN	B-CNN	EAVMF	ClassiGAN	Att-ClassiGAN
Precision	0.977	0.961	0.990	0.981	0.980
Recall	0.977	0.960	0.990	0.981	0.980
F1-score	0.977	0.960	0.990	0.981	0.980
NMSE	0.027	0.112	0.031	0.019	0.018
SSIM	0.969	0.876	0.964	0.979	0.983
Running Times	0.062	0.061	0.063	0.061	0.059

V. CONCLUSION

This study presents a further development of the original ClassiGAN architecture with attention modules to improve the ClassiGAN's ability of information processing. In addition to the use of an attention mechanism, the complexity of the ClassiGAN is also reduced, contributing to a faster computation speed. The Att-ClassiGAN effectively reconstructs images of handwritten numeric targets and accurately classifies them by learning the features directly from back-scattered measurements. The model is evaluated using a synthetic dataset comprising 3,000 samples. It achieves an average NMSE of 0.018 and an SSIM of 0.983 for the image reconstruction task. In terms of its performance on the classification task, the model obtained an average precision, recall, and F1-score of 0.980. Notably, Att-ClassiGAN also demonstrates a 97.57% reduction in average computation time compared to conventional CI-based methods. A comprehensive comparison with several state-of-the-art learning models is conducted to validate the effectiveness of the proposed approach. By performing image reconstruction and classification simultaneously without incurring additional computational costs, Att-ClassiGAN significantly enhances the efficiency of computational imaging systems operating at microwave frequencies.

REFERENCES

- [1] S. Song *et al.*, "Efficient image reconstruction methods based on structured sparsity for short-range radar," *IEEE Trans. Geosci. Remote Sens.*, pp. 1–1, 2024.
- [2] D. M. Sheen, D. L. McMakin, and T. E. Hall, "Three-dimensional Millimeter-wave Imaging for Concealed Weapon Detection," *IEEE Transactions on Microwave Theory and Techniques*, vol. 49, pp. 1581–1592, 2001.
- [3] S. Song *et al.*, "Efficient near-field radar microwave imaging based on joint constraints of low-rank and structured sparsity at low snr," *IEEE Trans. Microw. Theory Tech.*, pp. 1–16, 2024.
- [4] W. Xiong *et al.*, "Locating a moving source with unknown constant velocity during a short period of asynchronous toa collection," *IEEE Trans. Veh. Technol.*, pp. 1–5, 2025.
- [5] G. Zhang *et al.*, "Direct target localization with low-bit quantization in wireless sensor networks," *IEEE Trans. Signal Process.*, pp. 1–17, 2024.
- [6] O. Yurduseven *et al.*, "Frequency-diverse computational direction of arrival estimation technique," *Sci. Rep.*, vol. 9, no. 1, p. 16704, 2019.
- [7] J. He *et al.*, "Cramér-rao lower bound analysis for elliptic localization with random sensor placements," *IEEE Trans. Aerosp. Electron. Syst.*, vol. 60, no. 4, pp. 5587–5595, 2024.
- [8] G. Zhang *et al.*, "Direct target localization with quantized measurements in noncoherent distributed mimo radar systems," *IEEE Trans. Geosci. Remote Sens.*, vol. 61, pp. 1–18, 2023.
- [9] J. He, F. Yin, and H. C. So, "A framework for millimeter-wave multi-user slam and its low-cost realization," *Signal Processing*, vol. 209, p. 109018, 2023.
- [10] A. Mirbeik-Sabzevari, E. Oppelaar, R. Ashinoff, and N. Tavassolian, "High-Contrast, Low-Cost, 3-D Visualization of Skin Cancer Using Ultra-High-Resolution Millimeter-Wave Imaging," *IEEE Transactions on Medical Imaging*, vol. 38, no. 9, pp. 2188–2197, 2019.
- [11] O. Yurduseven *et al.*, "Frequency-diverse computational automotive radar technique for debris detection," *IEEE Sens. J.*, vol. 20, no. 22, pp. 13 167–13 177, 2020.
- [12] D. Sheen *et al.*, "Three-dimensional millimeter-wave imaging for concealed weapon detection," *IEEE Trans. Microw. Theory Tech.*, vol. 49, no. 9, pp. 1581–1592, 2001.
- [13] S. Song *et al.*, "An effective image reconstruction enhancement method with convolutional reweighting for near-field SAR," *IEEE Antennas Wirel. Propag. Lett.*, pp. 1–5, 2024.
- [14] A. Moreira *et al.*, "A tutorial on synthetic aperture radar," *IEEE Geosci. Remote Sens. Mag.*, vol. 1, no. 1, pp. 6–43, 2013.

- [15] J. Chen *et al.*, "Real-time processing of spaceborne sar data with nonlinear trajectory based on variable prf," *IEEE Trans. Geosci. Remote Sens.*, vol. 60, pp. 1–12, 2021.
- [16] M. García-Fernández *et al.*, "Array-based ground penetrating synthetic aperture radar on board an unmanned aerial vehicle for enhanced buried threats detection," *IEEE Trans. Geosci. Remote Sens.*, vol. 61, pp. 1–18, 2023.
- [17] G. Álvarez Narciandi *et al.*, "Dynamic metasurface antenna-based mills-cross aperture for 3D computational microwave imaging," *IEEE Antennas Wirel. Propag. Lett.*, pp. 1–5, 2024.
- [18] O. Yurduseven *et al.*, "Millimeter-wave spotlight imager using dynamic holographic metasurface antennas," *Opt. Exp.*, vol. 25, no. 15, pp. 18 230–18 249, 2017.
- [19] T. V. Hoang *et al.*, "Computational polarimetric imaging using two-dimensional dynamic metasurface apertures," *IEEE Open J. Antennas Propag.*, vol. 2, pp. 488–497, 2021.
- [20] A. Li *et al.*, "Frequency-diverse reflection metasurface antenna design for computational microwave imaging," *IEEE Open J. Antennas Propag.*, pp. 1–1, 2024.
- [21] M. Zhao *et al.*, "Dual-polarized frequency-diverse metaimager for computational polarimetric imaging," *IEEE Trans. Antennas Propag.*, vol. 72, no. 7, pp. 5479–5488, 2024.
- [22] T. V. Hoang *et al.*, "Spatial diversity improvement in frequency-diverse computational imaging with a multi-port antenna," *Results Phys.*, vol. 22, p. 103906, 2021.
- [23] M. Zhao *et al.*, "Towards a reconfigurable metacavity antenna for computational imaging and doa estimation," in *Proc. 2024 18th Eur. Conf. Antennas Propag.*, 2024, pp. 1–5.
- [24] T. Sleasman *et al.*, "Computational imaging with dynamic metasurfaces: A recipe for simple and low-cost microwave imaging," *IEEE Antennas Propag. Mag.*, vol. 64, no. 4, pp. 123–134, 2022.
- [25] O. Yurduseven *et al.*, "Design and simulation of a frequency-diverse aperture for imaging of human-scale targets," *IEEE Access*, vol. 4, pp. 5436–5451, 2016.
- [26] L. Li *et al.*, "Deepnis: Deep neural network for nonlinear electromagnetic inverse scattering," *IEEE Trans. Antennas Propag.*, vol. 67, no. 3, pp. 1819–1825, 2019.
- [27] R. Guo *et al.*, "A nonlinear model compression scheme based on variational autoencoder for microwave data inversion," *IEEE Trans. Antennas Propag.*, vol. 70, no. 11, pp. 11 059–11 069, 2022.
- [28] X. Bi *et al.*, "Diffusionemis: Diffusion model for 3-d electromagnetic inverse scattering," *IEEE Trans. Geosci. Remote Sens.*, vol. 62, pp. 1–12, 2024.
- [29] P. del Hougne *et al.*, "Learned integrated sensing pipeline: reconfigurable metasurface transceivers as trainable physical layer in an artificial neural network," *Adv. Sci.*, vol. 7, no. 3, p. 1901913, 2020.
- [30] Y. Qin *et al.*, "Breast imaging by convolutional neural networks from joint microwave and ultrasonic data," *IEEE Trans. Antennas Propag.*, vol. 70, no. 8, pp. 6265–6276, 2022.
- [31] Y. Sun *et al.*, "Hybrid data-driven ssm for interpretable and label-free mmwave channel prediction," *IEEE Trans. Mobile Comput.*, pp. 1–17, 2025.
- [32] R. Sharma, B. Deka, V. Fusco, and O. Yurduseven, "Integrated convolutional neural networks for joint super-resolution and classification of radar images," *Pattern Recognit.*, vol. 150, p. 110351, 2024.
- [33] M. Tan *et al.*, "Electromagnetic imaging boosted visual object recognition under difficult visual conditions," *IEEE Trans. Geosci. Remote Sens.*, vol. 61, pp. 1–12, 2023.
- [34] J. Zhang, G. Álvarez Narciandi, M. García-Fernández, R. Sharma, J. Zhang, P. del Hougne, M. Ali Babar Abbasi, and O. Yurduseven, "Classigan: Joint image reconstruction and classification in computational microwave imaging," *IEEE Transactions on Radar Systems*, vol. 3, pp. 441–452, 2025.
- [35] M. García-Fernández *et al.*, "Single channel frequency-diverse computational imaging system for through-the-wall sensing," *IEEE Trans. Geosci. Remote Sens.*, vol. 62, pp. 1–10, 2024.
- [36] J. Hunt *et al.*, "Metamaterial apertures for computational imaging," *Science*, vol. 339, no. 6117, pp. 310–313, 2013.
- [37] G. Lipworth *et al.*, "Comprehensive simulation platform for a metamaterial imaging system," *Appl. Opt.*, vol. 54, no. 31, pp. 9343–9353, 2015.
- [38] T. Sleasman *et al.*, "Experimental synthetic aperture radar with dynamic metasurfaces," *IEEE Trans. Antennas Propag.*, vol. 65, no. 12, pp. 6864–6877, 2017.
- [39] Y. LeCun *et al.*, "Gradient-based learning applied to document recognition," *Proc. IEEE*, vol. 86, no. 11, pp. 2278–2324, 1998.
- [40] A. Mao *et al.*, "Cross-entropy loss functions: Theoretical analysis and applications," in *Proc. Int. Conf. Mach. Learn.*, vol. 202, 2023, pp. 23 803–23 828.
- [41] J. Zhang *et al.*, "Sensing matrix prediction from back-scattered data in computational microwave imaging," *IEEE Antennas Wirel. Propag. Lett.*, pp. 1–5, 2024.
- [42] P. Isola *et al.*, "Image-to-image translation with conditional adversarial networks," in *Proc. IEEE Conf. Comput. Vision Pattern Recognit.*, 2017, pp. 5967–5976.
- [43] A. Kendall *et al.*, "Multi-task learning using uncertainty to weigh losses for scene geometry and semantics," in *Proc. IEEE conf. comput. vision pattern recognit.*, 2018, pp. 7482–7491.
- [44] T. Gong *et al.*, "A comparison of loss weighting strategies for multi task learning in deep neural networks," *IEEE Access*, vol. 7, pp. 141 627–141 632, 2019.
- [45] J. Zhang *et al.*, "Deep learning for sensing matrix prediction in computational microwave imaging with coded-apertures," *IEEE Access*, vol. 12, pp. 16 844–16 855, 2024.
- [46] Y. Wang *et al.*, "A convolutional neural network method based on adam optimizer with power-exponential learning rate for bearing fault diagnosis," *J. Vibroengineering*, vol. 24, no. 4, pp. 666–678, 2022.
- [47] A. M. Molaei *et al.*, "Fast processing approach for near-field terahertz imaging with linear sparse periodic array," *IEEE Sensors J.*, vol. 22, no. 5, pp. 4410–4424, 2022.
- [48] R. Sharma *et al.*, "3-d super-resolution of coded aperture millimeter-wave images using complex-valued convolutional neural network," *IEEE Sensors J.*, vol. 22, no. 21, pp. 20 921–20 936, 2022.